COMPOSITIONALLY TUNED HIGH-ENTROPY LI-GARNET ELECTROLYTE FOR ADVANCED SOLID-STATE BATTERIES

Asish Kumar Das[a,*] and Sunil Kumar [a,**]

[a]Department of Metallurgical Engineering and Materials Science, Indian Institute of Technology Indore,

Simrol, 453552, India

**Corresponding author E-mail: sunil@iiti.ac.in

*Corresponding author E-mail: phd2201105011@iiti.ac.in

Abstract

The advancement of all-solid-state lithium batteries (ASSLBs) hinges on developing highly conductive and chemically stable solid electrolytes. High-entropy ceramics leveraged from high configurational entropy and synergistic interactions among the elements have emerged as a rapidly expanding class of high-entropy materials, attracting significant attention due to their exceptional properties. Here, a high-entropy Li-stuffed garnet (HEG) solid electrolyte, $Li_7La_3Zr_{0.5}Hf_{0.5}Sc_{0.5}Nb_{0.25}Ta_{0.25}O_{12}$, crystallizing in a highly Li^+ conductive (~ 1.25×10^{-4} S cm^{-1} at room temperature) cubic phase, is reported. Electrochemical evaluations demonstrate excellent stability against lithium metal, with symmetric Li|HEG|Li cells sustaining stable Li plating/stripping beyond 550 cycles at 0.4 mA cm^{-2}. Furthermore, full-cell integration with $LiFePO_4$ (LFP) cathodes exhibits high capacity retention (~99% over 500 cycles), confirming its potential for high-performance ASSLBs. Further, the HEG solid electrolyte is compatible with high voltage $LiMn_2O_4$ cathode (mass loading ~ 16.6 mg cm^{-2}), retaining 96% capacity over 100 cycles (at 0.2C). Our findings establish a framework for tailoring high-entropy garnet electrolytes, paving the way for next-generation solid-state battery technologies.

Keywords: *all-solid-state lithium batteries; high-entropy; garnet; solid electrolyte; ionic conductivity*.

1. Introduction

The swift escalation of worldwide energy demands and the urgent necessity to tackle environmental issues have propelled the quest for sustainable and effective energy storage systems. Lithium-ion batteries (LIBs) have revolutionized the field of portable electronics and electric vehicles, primarily due to their high energy density and prolonged lifespan.[1-3] However, traditional LIBs, which employ liquid electrolytes, suffer from inherent challenges such as flammability, leakage, and dendrite-induced short circuits, raising concerns about their safety and longevity. This has driven the development of all-solid-state lithium batteries (ASSLBs), which promise enhanced safety, higher energy densities, and superior thermal stability.[4-6] At the core of this transformative technology lies the solid-state electrolyte (SSE), a critical component dictating the performance and feasibility of ASSLBs.

The concept of high-entropy materials (HEMs) has emerged as a revolutionary strategy in materials science, offering unparalleled opportunities to tailor properties by leveraging compositional complexity.[7-10] High-entropy materials, characterized by the incorporation of multiple principal elements in near-equimolar ratios, exhibit unique characteristics such as lattice distortion and enhanced thermal stability.[11] High configurational entropy boosts the electrochemical performance in the Na^+/Li^+ electrode materials by delaying detrimental structural phase transformations and abstaining from particle degradation during charge-discharge cycles.[12-14] Despite the extensive exploration of high-entropy electrode materials, reports on high-entropy SSEs remain scarce. This presents opportunities for further research to harness the advantages of high-entropy design to develop innovative SSEs with superior properties.[15] High entropy offers significant potential for SSEs, as the variation in ionic size and electronegativity among diverse elements can influence lattice parameters and adjust the local structure.[16-19] This diversity leads to occupational disorder in the sublattice and fosters synergistic interactions between cations and anions, potentially enhancing ionic conductivity. Furthermore, as demonstrated by high-entropy polyanionic ion conductors, increasing the number of species in SSEs can boost both configurational and vibrational entropy, thereby lowering the energy barrier for ion migration.[12, 20]

Solid-state batteries with inorganic electrolytes offer high safety and energy density, primarily because of their non-flammability nature and the potential for using lithium metal anodes. High Li^+ conductivity and chemical stability with Li metal are crucial for solid electrolytes, especially for garnet-type materials like $Li_7La_3Zr_2O_{12}$ (LLZO), which show promising conductivity ($>10^{-4}$ S/cm at room temperature).[21-23] Stabilizing the

high-conductivity cubic phase over the less conductive tetragonal phase (conductivity ~10^{-6} S cm^{-1}) is necessary, as the cubic structure provides low-energy landscapes inside the crystal structure, facilitating fast lithium-ion migration pathways. However, lithium-lithium repulsion at Li2 (96h) sites in the cubic phase can destabilize it at higher lithium contents, resulting in a tetragonal phase. The strategy of aliovalent doping (e.g., with Al or Ga at Li sites or Nb or Ta at Zr sites) has been employed extensively to stabilize the cubic phase by creating Li-vacancies that can reduce Li–Li repulsion. For example, extensive studies on Ta-doped LLZO show a critical vacancy concentration (~0.4–0.5) essential for cubic phase stabilization.[24-28]

It has been reported that a high lithium content in the garnet composition is conducive to better interfacial contact with lithium metal.[29] The introduction of site disorderliness has garnered much attention in recent years to stabilize various phases compared to their low-entropy counterparts.[30-31] However, few garnet materials have been reported in the literature with a Li composition of 7.0 per formula unit, except $Li_7La_3Zr_2O_{12}$, which is very difficult to obtain in the cubic phase.[25, 29] This work reports the synthesis and characterization of cubic-phase *high entropy garnet* (~−1.56 R),

$$S_{cofig}\,at\ Zr-site = -R\left[\sum_{i=1}^{N} x_i\,ln\,x_i\right]_{Zr-site}$$
$$= -R\left[\left(3\times\left[\frac{0.5}{2}\times\ln\left[\frac{0.5}{2}\right]\right]\right)+\left(2\times\left[\frac{0.25}{2}\times\ln\left[\frac{0.25}{2}\right]\right]\right)\right] = -1.55958\,R,$$

with a new chemical composition of $Li_7La_3Zr_{0.5}Hf_{0.5}Sc_{0.5}Nb_{0.25}Ta_{0.25}O_{12}$ (HEG), achieved through the disorderliness resulting from five different cations at the Zr-site. The configurational entropy arises solely from the statistically distributed cations at the Zr-site, with no contributions from the La- and O-sites due to the absence of dopants. HEG has a cubic structure (space group: $Ia\bar{3}d$) without any additional lithium vacancies. The high ionic conductivity, low electronic conductivity, and extended longevity of the HEG electrolyte offer valuable insights for developing advanced SSEs.

2. Experimental Details

2.1 High Entropy Garnet Synthesis:

The high entropy garnet $Li_7La_3Zr_{0.5}Hf_{0.5}Sc_{0.5}Nb_{0.25}Ta_{0.25}O_{12}$ (HEG) was synthesized by the solid-state reaction method using lithium hydroxide (LiOH), lanthanum oxide (La_2O_3), zirconium oxide (ZrO_2), Hafnium oxide (HfO_2), tantalum oxide (Ta_2O_5), scandium oxide (Sc_2O_3), and niobium oxide (Nb_2O_5). To compensate for the lithium oxide volatilization during sintering, an excess of 15 wt.% LiOH was used. The precursors were mixed thoroughly in an agate mortar-pestle by hand for 1 h, followed by ball-milling in isopropanol medium in a zirconia jar for 12 h (15-minute rest between

two cycles) at 300 rpm. The dried mixture was pelletized using a 16 mm diameter stainless steel die set with a uniaxial pressure of 250 MPa. These cold-pressed pellets, completely covered with the powder of the same composition, were calcined at different temperatures for 12 h. The calcined powder with cubic phase was further ball-milled, and 16 mm cylindrical green bodies were formed by applying 250 MPa uniaxially. The green bodies were buried under the same calcined powder and underwent sintering at 1150 °C (heating rate: 5 °C/min, dwelling time: 2h, cooling rate: furnace cooled). The sintered pellets were polished with sandpaper with various grits (#800, #1500, #2500, and #5000). 1M HCl acid was used to clean the pellet's surface for 2 min. and then washed with ethanol, followed by transferring into an Ar-filled M-Braun glovebox (O_2 and H_2O < 0.1 ppm) for further characterizations.

2.2 Coin cell fabrication

Symmetric cells: The symmetric lithium cells, denoted as Li|HEG|Li, were assembled using lithium metal on either side of the pellet, and PEO/LiTFSI thin film was used for better interface contact at the electrode-electrolyte interface. The fabricated cells were heated at 60 °C for 1 h to improve the adhesion of the HEG pellet surface to the lithium metal before further characterization.

Full cells: Slurries (NMP solvent) of $LiFePO_4$ (LFP) cathodes (PVDF binder: electronic conducting Ketjen black: $LiFePO_4$ active material weight ratio ~ 10: 10: 80) were applied onto aluminum current collectors and then dried in a vacuum oven at 120 °C for 24 hours. After drying, the punched circular cathodes (area: ~78 mm^2, active material: 1-2 mg cm^{-2}) were transferred into the Ar-filled glovebox. For the full-cell fabrication, a PEO/LiTFSI membrane was sandwiched between the lithium metal and pellet and heated at 60 °C for 1 h, and the LFP cathode sheet and the $LiMn_2O_4$ cathode sheet (diameter: 10 mm, commercially purchased from MTI corporation, active material loading: 16.6 mg cm^{-2}) was attached to the other side of the pellet. The whole configuration was crimped in a coin cell CR2032 using a hydraulic crimping machine inside the glovebox. A 5 µL liquid electrolyte (1M $LiPF_6$ in PC) was used to ameliorate the lithium-ion conduction on the cathode side.

2.3 Characterization

The material characterization was conducted using various techniques. X-ray diffraction (XRD) analysis was performed on an Empyrean X-ray diffractometer equipped with Cu-K_α radiation (wavelength: 1.54 Å, current: 40 mA, voltage: 30 kV), covering a 2θ range of 10° to 60°. Crystallographic parameters were determined from the XRD data using Rietveld refinement with the TOPAS academic version 6 software.[32] The relative density of the sintered samples was measured via Archimedes' principle using Xylene

as the fluid. The microstructural features of the synthesized samples and elemental mapping were observed using a JEOL-7610+ field emission scanning electron microscope (FE-SEM). The complex impedance spectroscopy data was taken in a Biologic electrochemical workstation (SP-50e) across the frequency range of 10 mHz to 1 MHz with a sinus voltage amplitude of 10 mV on HEG solid electrolyte pellets (Ag electrodes painted by color brush on both sides of polished pellets and cured at 750 °C for 2 minutes), lithium symmetric and full cells (cathode: $LiFePO_4$, Anode: Lithium metal). The chronoamperometry test was performed on Ag|HEG|Ag configuration to determine the electronic conductivity using a Keithley Source Meter Unit (Model 2450-EC). Distribution of relaxation times (DRT) analysis of impedance data was carried out using DRT tools.[33-36] Constant current charge-discharge measurements were carried out on lithium symmetric and full cells using a Neware BTS4000-5V20mA battery tester. Except for impedance measurements and charge-discharge tests, all electrical and electrochemical experiments were performed at room temperature (25 °C).

3. Results and Discussions

The cubic-phase $Li_7La_3Zr_{0.5}Hf_{0.5}Sc_{0.5}Nb_{0.25}Ta_{0.25}O_{12}$ (HEG) was synthesized leveraging the mixed oxidation states of Hf (+4), Sc (+3), Nb (+5), and Ta (+5) via a solid-state reaction route. X-ray diffraction (XRD) was employed to explore the structural evolution of HEG with varying calcination temperatures. Figure 1(a) shows the XRD patterns obtained for the calcined HEG samples at different temperatures (700 °C, 800 °C, 900 °C, 950 °C, and 1000 °C) with a dwelling time of ~ 12 h. At 700 °C and 800 °C, the XRD pattern revealed the tetragonal structure of HEG, as the thermal energy was insufficient to overcome the enthalpic barriers for cubic stabilization. No tetragonal nature in the crystal structure was found for the HEG calcined at 900 °C and 950 °C, but the tetragonal structure again appeared for the sample calcined at 1000 °C. This suggests that Gibbs' free energy attained a minimum value at around 900 °C and 950 °C, which impeded the cubic to tetragonal phase transformation upon cooling from the calcination temperature to room temperature. The high lithium loss at 1000 °C caused the destabilization of the cubic phase, leading to deviation from the ideal Li:La:M stoichiometry and formation of secondary phases. Further, the calcined HEG powder at 950 °C contained fewer impurities than the powder heated at 900 °C. The narrow thermal window (900–950 °C) within which the cubic phase is stabilized reflects a delicate balance between enthalpy and configurational entropy contributions to Gibbs free energy ($\Delta G = \Delta H - T\Delta S$). At this temperature range, the system minimizes ΔG, favoring the cubic phase due to high configurational entropy induced by the multi-cation (Zr/Hf/Ta/Nb/Sc) mixing at the 16a octahedral site.[20, 29] Notably, the absence

of tetragonal distortions in this range implies suppression of Li-site ordering, which typically drives tetragonal symmetry at lower temperatures.

As presented in Figure 1(b), the Rietveld refinement of the powder XRD data indicates that the synthesized HEG (T: 950 °C, dwelling time: 12 h) exhibits a cubic structure (space group: $Ia\bar{3}d$, space group number: 230, lattice parameter, a = 12.9284 Å, and unit cell volume, V = 2160.918 Å^3), consistent with other reported cubic garnet compounds.[37-39] These results demonstrate the role of disorderliness in the miscibility of multiple cations at the Zr-site within the cubic structure, even with a facile synthesis procedure. Notably, the ionic radius of Zr^{4+} (0.72 Å) is larger than that of the average ionic radius (~0.68 Å) of Hf^{4+}, Ta^{5+}, Sc^{3+}, and Nb^{5+} in a six-coordination environment, resulting in a slight decrease in the lattice parameter a for HEG (~12.9284 Å) compared to $Li_7La_3Zr_2O_{12}$ (~12.9682 Å).[40] During Rietveld refinement, both tetragonal and cubic structural models were employed initially, with the refinement outcomes summarized in Table S1.[32]. The analysis unequivocally confirms a pure cubic phase, facilitated by partial substitution of Hf^{4+}, Ta^{5+}, Sc^{3+}, and Nb^{5+} for Zr^{4+} within the garnet structure. Also, the lack of superlattice reflections in XRD further confirms the disordered nature of the Zr-site cations. In this cubic garnet phase, lithium ions exhibit a random distribution across two Wyckoff positions (the 24d site and the distorted 96h site). Generally, stabilization of the cubic phase in lithium-stuffed garnet electrolytes ($Li_7La_3Zr_2O_{12}$) necessitates a degree of lithium disorder, driven by the presence of Li vacancies (approximately 0.4–0.5 atoms per formula unit), to mitigate strong Li–Li Coulombic repulsions[24]. But in the HEG sample, the cubic phase was obtained without creating any lithium vacancies, and it is attributed to the multi-cationic potential disorderliness obstructing the cubic-to-tetragonal phase transformation. The occupancy at the 96h site was determined to be ~0.46, which may be beneficial for easier Li^+ transport via a concerted cationic motion inside the crystal structure.[41]

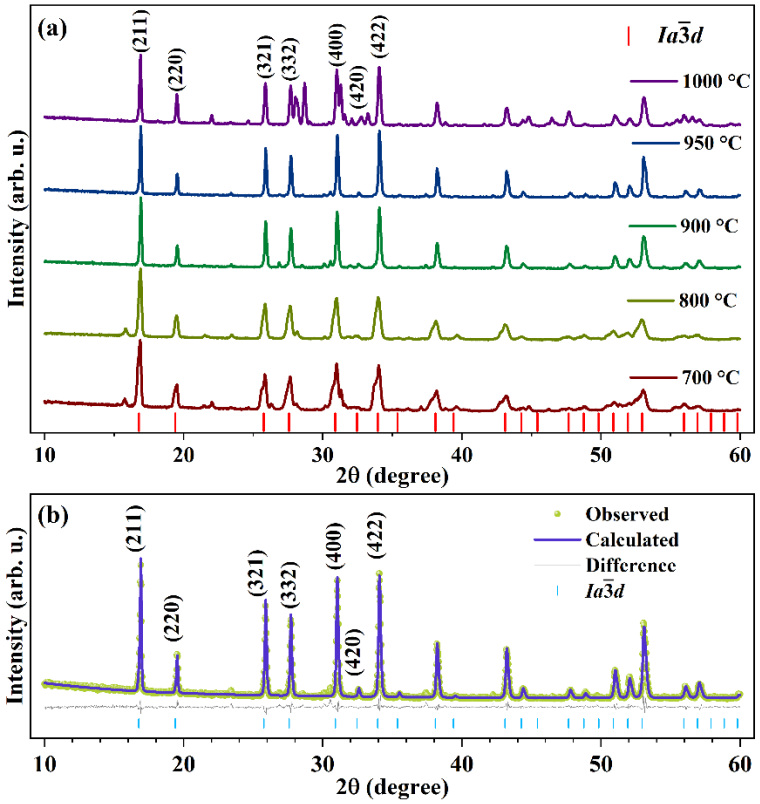

Figure 1: (a) Room temperature X-ray diffraction patterns of HEG powder calcined at different temperatures. (b) The Rietveld refinement profile of powder X-ray diffraction data of HEG powder calcined at 950 °C.

The microstructural information obtained from the SEM image (Figure 2(a)) affirmed the high densification of the HEG ceramics pellet, which is further corroborated by a high relative density of ~ 93% calculated using Archimedes' method. The image at higher magnification in Figure 2(b) showed the grains' sizes to be approximately ~ 5-6 μm. The dense nature of the HEG solid electrolyte is essential to obstruct the lithium dendrite-mediated electrical breakdown of the solid-state cells. The SEM-energy dispersive spectroscopy image (Figure 3(c-j)) presents the homogeneous distribution of zirconium, hafnium, scandium, tantalum, and niobium across the particles, validating the successful substitution of multiple substituents into the material's composition. Also, the SEM-EDS technique was utilized to estimate the approximate atomic ratios of the elements present, excluding lithium and oxygen. The atomic ratio obtained (La: Zr: Hf: Sc: Ta: Nb= 6: 0.09: 0.8: 0.11: 0.06: 0.04) closely aligns with the intended composition.

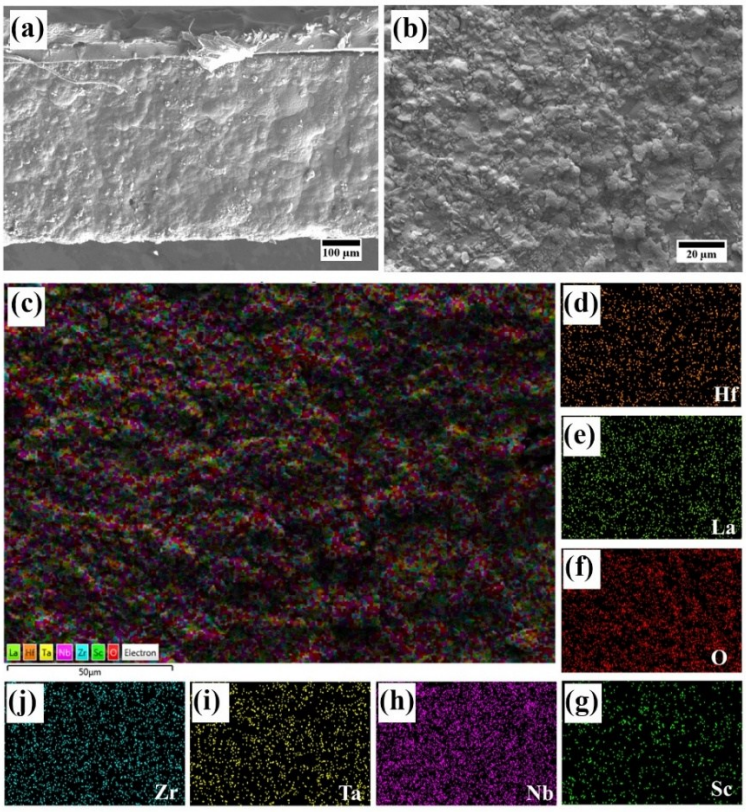

Figure 2: (a) The electron microscopy image of a cross-section of the HEG pellet. (b) The magnified version shows the microstructure of the cross-section of the HEG pellet. (c)-(j) The electron dispersive spectroscopy mappings of constituent elements of the HEG solid electrolyte.

HEG, as a solid electrolyte, must exhibit high ionic conductivity and low electronic conductivity to be a viable option for solid-state lithium batteries. To analyze electrical properties, complex impedance spectroscopy (CIS) and direct current polarization tests were conducted on Ag|HEG|Ag cell configurations. Figures 3(a1-a6) present the evolution of Nyquist plots (real impedance vs. imaginary impedance presented in orthonormal axes) of HEG at different temperatures, including the room temperature data. In the room temperature Nyquist, a semicircular feature was observed at the high frequency corresponding to the lithium-ions movement within the solid electrolyte, whereas the long tail in the low frequency domain denotes the lithium ions impermeability through the Ag electrodes, indicating that HEG functions primarily as an ionic conductor. The impedance data was modeled using a typical 3-component equivalent electrical circuit consisting of one resistor (R) and two constant phase elements (Q1 & Q2). Q1 and R were connected in parallel, and Q2 was joined with this parallel circuit in series connection. The grain and grain boundary contributions could not be deconvoluted from the Nyquist plots at room temperature and higher

temperatures. The conductivity of the HEG solid electrolyte was determined to be ~1.25 × 10^{-4} S cm^{-1} at room temperature (conductivity was calculated using the modeled 'R' and the pellets' dimensions). As the temperature increased, the lithium-ion kinetics inside the solid electrolyte got agitated due to the thermal energy, and the semi-circular feature gradually diminished. The calculated conductivities at different temperatures were used to fit the Arrhenius equation as,

$$\sigma(T) = \sigma_0 e^{-\frac{E_A}{k_B T}} \quad (1)$$

where T and k_B denote the absolute temperature and Boltzmann constant, σ_0 and E_A represent the pre-exponential factor and lithium-ion migration energy barrier, respectively. The value of E_A for HEG solid electrolyte, obtained from the Arrhenius plot's linear fitting (Figure 3(b)), was found to be 0.41 ± 0.02 eV.

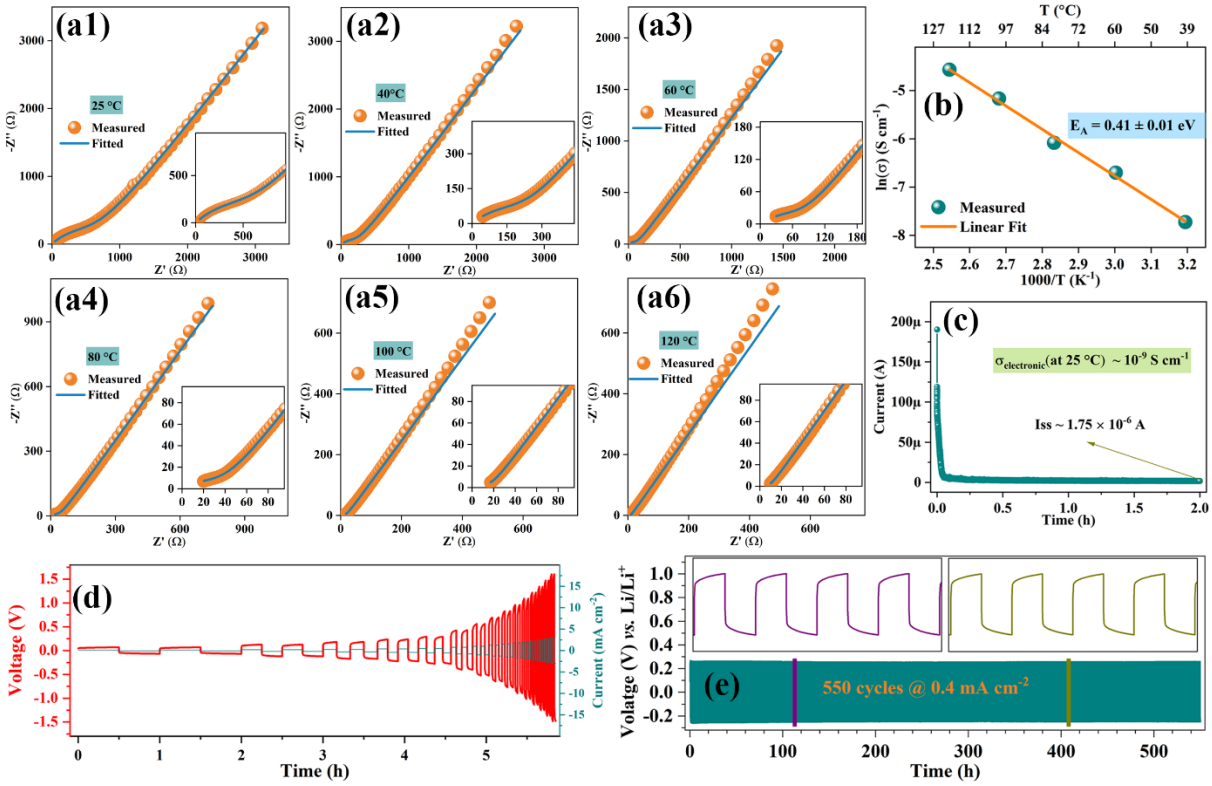

Figure 3: (a1)-(a6) The Nyquist plots of HEG solid electrolyte at different temperatures. (b) Linear fitting of Arrhenius plot of conductivity at different temperatures of HEG solid electrolyte. (c) Chronoamperometry measurement of HEG solid electrolyte at room temperature under a DC voltage of 1 V. (d) The lithium plating-stripping overpotential curves at different current densities. (e) The lithium plating/stripping behavior at 0.4 mA cm^{-2} for 550 h.

As shown in Figure 3(c), during the direct current polarization test, the current decreased rapidly under a steady 1 V and attained a constant current value of ~1.75 µA. The initial current comes from both the lithium-ion and electronic conduction, which is

exponentially reduced to a constant value because of the blocking of lithium ions at the Ag electrode interface. The steady-state current stems from electronic conduction only. The dimensions of the solid electrolyte pellet were used to calculate the electronic conductivity using the equation. The electronic conductivity of HEG was measured to be 1.5×10^{-9} S cm^{-1}, confirming its excellent electronically insulating properties as a solid-state electrolyte (SSE) membrane, which is essential for long-term cyclability and lithium dendrite suppression.

The electrochemical properties of HEG were investigated by assembling symmetric and full cells to assess its performance. The symmetric cells were fabricated by sandwiching lithium metal chips on both sides of the HEG solid electrolyte pellet with a PEO-LITFSI buffer layer between the lithium metal and HEG pellet. The Nyquist plots shown in Figure S1 illustrate that there was a substantial reduction in the total resistance of the symmetric cell upon the introduction of the PEO-LITFSI buffer layer. As presented in Figure 3(d), the symmetric cell underwent lithium plating-stripping at different current densities to determine the critical current density, which was found to be above ~3 mA cm^{-2} (considering the critical current density at which the maximum current the solid-state electrolyte can sustain its electrical integrity). Although the HEG symmetric cell withstands a current of 3 mA cm^{-2}, the over-potential value crossed 1 V, which makes it impractical to run the cell at such currents. Further, to assess the long cycling durability of the solid electrolyte, galvanostatic charging-discharging was performed for 550 cycles at 0.4 mA cm^{-2} (Figure 3(e)). The cell exhibited stable cycling without any significant polarization growth or any sign of soft/hard breakdown, demonstrating the excellent durability of the HEG electrolyte for practical applications. Figure S2 presents the Nyquist plots for Li|HEG|Li cells obtained before and after the lithium plating-stripping for 550 cycles, which corroborates the stable cycling along with no sign of micro short-circuits induced by lithium dendrites.

For full-cell tests, a $LiFePO_4$ cathode was used to assemble Li|HEG|$LiFePO_4$ full cells. Figure 4(a) presents specific capacity-potential curves at different C-rates at 25 °C (1C = 170 mAh g^{-1}). The full cell delivered a high discharge specific capacity of ~154 mAh g^{-1} at 0.1C rate, which gradually reduced to 64 mAh g^{-1} at 0.8C with an increased polarization potential. To demonstrate the full-cell performance for a longer duration, the charge-discharge test was performed at a constant current equivalent to the 0.5C rate for 500 cycles (Figure 4(e). Interestingly, the discharge-specific capacity of ~102 mAh g^{-1} in the 1st cycle increased initially (for 55 cycles) to a maximum of 110 mAh g^{-1}; thereafter, it decreased gradually with ~0.014% capacity loss per cycle upon further cycling. In comparison, the control cell with $LiFePO_4$ cathode exhibited a high capacity of ~ 161 mAh g^{-1} at 0.2C, which reduced to 135 mAh g^{-1} at 0.8C rate, with a relatively

lower polarization potential than our reported cell with HEG pellet (Figure S3). But our cell outperformed the control cell in the cyclability. The control cell delivered a capacity retention of ~ 97.3% after 50 cycles, which is lower than our reported cell with the HEG pellet (Figure S4). It is important to note that there is an increase in the capacity in the initial cycles in our reported cell, which was absent from the control cell.

Figure 4(f) demonstrates the minimal variation of nominal charge and discharge voltage with cycling, indicating the invariability of the total resistance of full cells during cycling. Generally, interfacial resistance due to sluggish lithium-ion kinetics dominates the overall cell resistance during cycling, as shown in Figure 4(g). In addition, the full cell demonstrated typical charging-discharging curves with excellent cycling stability and an excellent columbic efficiency of ~100% over 500 cycles (Figure 4(e)). These results suggest that the high ionic conductivity of HEG solid electrolyte, along with its ability to reduce the driving force for Li nucleation and its low electronic conductivity, which inhibits the growth of Li dendrites, contributes significantly to the commendable long-term cycling stability of HEG in both symmetric and full cells.

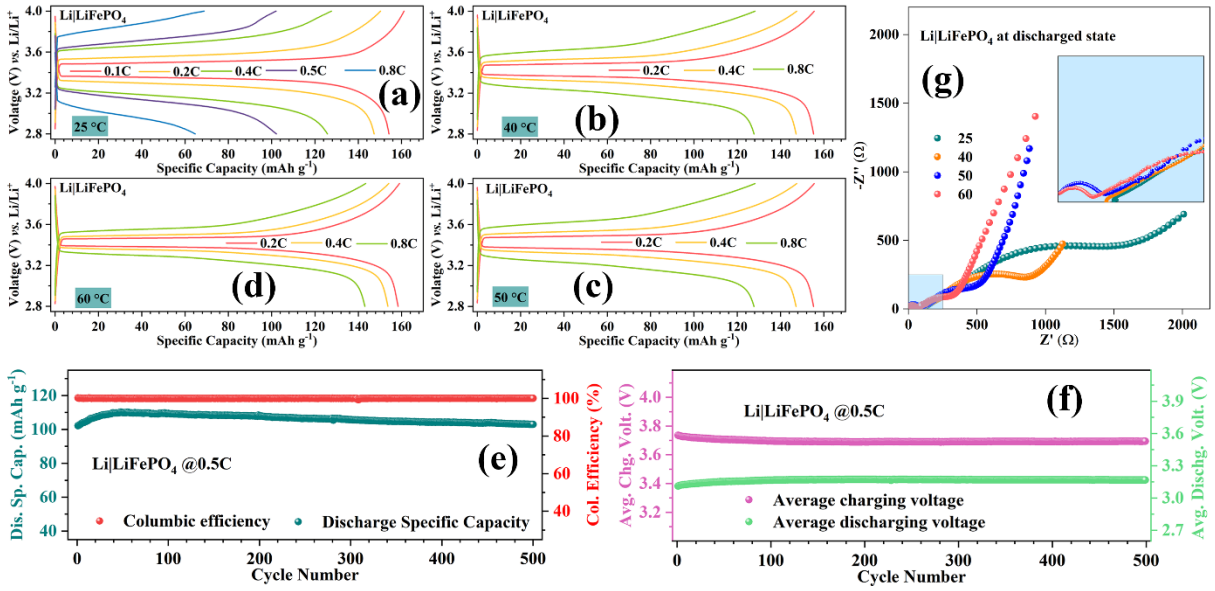

Figure 4: (a) The specific capacity-voltage curves of Li | LiFePO4 cell at different C rates at 25 °C. (b) The specific capacity-voltage curves of Li | LiFePO4 cell at different C rates at 40 °C. (c) The specific capacity-voltage curves of Li | LiFePO4 cell at different C rates at 50 °C. (d) The specific capacity-voltage curves of Li | LiFePO4 cell at different C rates at 60 °C. (e) The long-term cyclability of Li | LiFePO4 cell at 0.5C at 25 °C. (f) The evolution of average charging and discharging voltage of Li | $LiFePO_4$ cell with cycling. (g) The Nyquist plots of Li | $LiFePO_4$ cell at different temperatures at the discharged state.

To assess the impact of temperature on the solid-state battery's performance, constant charge-discharge tests at various current densities were conducted at 40 °C, 50 °C, and 60 °C. The results are depicted in Figures 4(b), 4(c), and 4(d). There is a substantial decrease in the polarization potential at various C rates with the increase in

temperature. At 0.8C, due to high polarization potential, the capacity obtained at room temperature was only ~64 mAh g^{-1}, which improved to ~142 mAh g^{-1} at 60 °C. The Nyquist plots of LFP cells at different temperatures (Figure 4(g)) also showed a change in both the electrolyte resistance and non-electrolyte resistance (charge transfer + interfacial resistance). Lithium-ion kinetics within the electrolyte, passivation layer, and cathode were positively correlated with temperature. Figure 5(a) presents the DRT (distribution of relaxation times) analysis of EIS data of Li|$LiFePO_4$ cell at different temperatures. Typically, the lower relaxation time indicates faster lithium-ion conduction. With the increase in temperature, there were clear shifts in the relaxation peaks to the lower relaxation time. Further, the relaxation time distribution curves at 50 °C and 60 °C were a bit different than those at 25 °C and 40 °C. This phenomenon could be attributed to a drastic change in the lithium-ion conduction mechanism at the Li-PEO/LiTFSI-HEG interface. The PEO polymer is known to have a very low melting temperature around 60 °C, which can be lowered due to the coin cell pressure.[42]

To evaluate the performance of the fabricated solid electrolyte with high-voltage cathode materials, $LiMn_2O_4$ (LMO) cells, with HEG as the electrolyte, were tested under varying current densities and extended cycling conditions. At 0.1C, the LMO cell exhibited a discharge specific capacity of ~105 mAh g^{-1}, aligning closely with its practical rated capacity of ~110 mAh g^{-1}. However, as the current density increased, the capacity progressively decreased, measuring ~67 mAh g^{-1} at ~0.2C, 47 mAh g^{-1} at 0.3C, and only ~32 mAh g^{-1} at ~0.5C (Figure 5(b)). It is important to note that loading for LMO is 16.6 mg cm^{-2}; accordingly, the current density at a given C rate is much higher for the LMO cell than for the LFP cell. This decline in specific capacity was accompanied by a reduction in energy efficiency, underscoring the challenges posed by higher current densities.

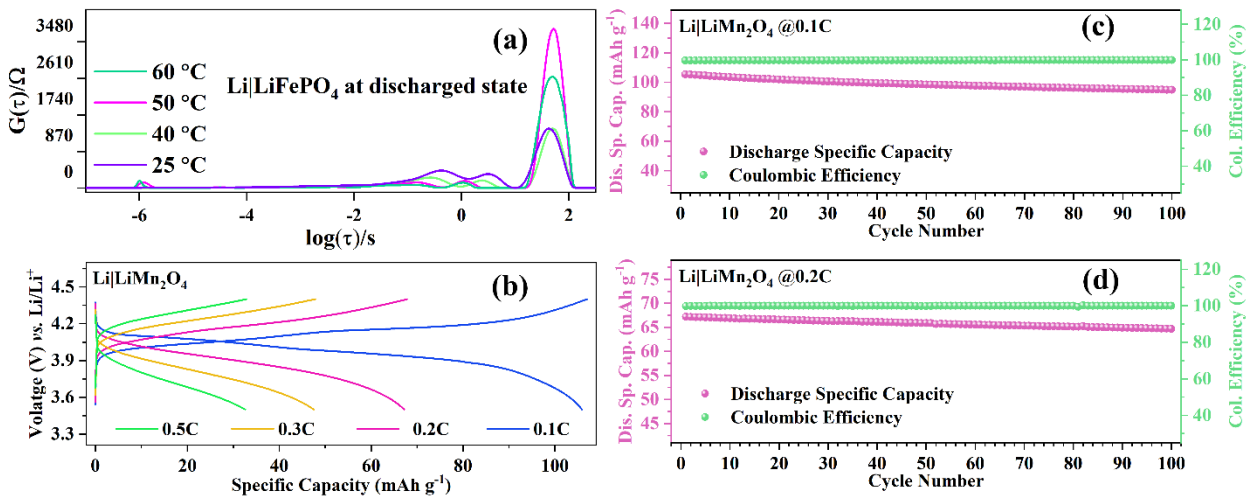

Figure 5: (a) The distribution of relaxation times for discharged (to 2.8 V) Li | $LiFePO_4$ cells at different temperatures. (b) The specific capacity-voltage curves of the Li | $LiMn_2O_4$ cell at different C rates at 25 °C. (c) & (d) The long-term cyclability of Li | $LiMn_2O_4$ cell at 0.1C & 0.2C at 25 °C, respectively.

To probe the long-term cycling stability, a key indicator of cell durability, LMO cells were charged and discharged at 0.1C and 0.2C, with performance metrics presented in Figures 5(c) and 5(d), respectively. During cycling, the cells exhibited gradual capacity fading over 100 cycles (~90% capacity retention at 0.1C and only ~4% capacity loss at 0.2C). In contrast, the control cell employing liquid electrolyte with a $LiMn_2O_4$ cathode exhibited consistently higher capacities across all C-rates, accompanied by a relatively lower polarization potential compared to the cells incorporating the HEG solid electrolyte (Figure S5). Specifically, the control cell delivered a capacity of ~ 69 mAh g^{-1} at 0.5C, which is significantly higher than that obtained with the HEG-based solid-state configuration. The reduced capacity in the latter can be primarily attributed to the increased polarization potential, likely stemming from interfacial resistance and ionic transport limitations in the solid-state architecture. Importantly, both the control and HEG-based cells demonstrated comparable cyclability at 0.1C-rate (Figure S6), suggesting that long-term performance degradation is not predominantly dictated by the solid electrolyte. These observations are likely a consequence of the continuous growth of the solid electrolyte interphase (SEI) and microstructural degradation of the LMO cathode, including cracking. Despite these challenges, the coulombic efficiency remained remarkably high ~99.99% at both 0.1C and 0.2C rates, indicative of the exceptionally low electronic conductivity of the ceramic electrolyte, as discussed earlier.

4. Conclusions

In summary, a high-entropy Li-stuffed garnet was successfully synthesized with five different cations (Zr^{4+}, Hf^{4+}, Ta^{5+}, Sc^{3+}, and Nb^{5+}) sharing the Zr-site within the crystal framework. This high configurational entropy stabilized the highly conductive cubic phase without requiring lithium vacancies. The resulting HEG composition ($Li_7La_3Zr_{0.5}Hf_{0.5}Sc_{0.5}Nb_{0.25}Ta_{0.25}O_{12}$) exhibits a room-temperature ionic conductivity of 1.25×10^{-4} S cm^{-1} and low electronic conductivity of ~10^{-9} S cm^{-1}, ensuring efficient Li-ion transport while preventing dendrite-induced failures. Combining high relative density, high ionic conductivity, and low electronic conductivity, HEG demonstrates significant durability, with the symmetric cell exhibiting stable cycling for 550 hours. Electrochemical performance assessments reveal stable long-term cycling in Li|HEG|Li, Li|HEG|$LiFePO_4$, and Li|HEG|$LiMn_2O_4$ configurations, demonstrating high cycling stability, stable interfacial resistance, and excellent compatibility with high-voltage cathodes. The suppression of Li dendrites and high-temperature resilience further solidifies HEG's promise for next-generation safe and high-energy-density solid-state batteries. Future efforts will focus on further optimizing ionic conductivity and interfacial compatibility to unlock its full potential in commercial battery applications.

Conflicts of Interest

There are no conflicts of interest to declare.

Data Availability Statement

The data that support the findings of this study are available from the corresponding authors upon reasonable request.

Credit author statement

Asish Kumar Das: Conceptualisation, Methodology, Investigation, Funding acquisition, Data curation, Formal analysis, Writing - Original Draft; **Sunil Kumar:** Funding acquisition, Supervision, Resources, Project administration, Validation, Writing - Review & Editing.

Acknowledgments

The author (AKD) thanks the Ministry of Education, Government of India, for the Prime Minister's Research Fellowship (PMRF) (PMRF ID - 2102737). The authors gratefully acknowledge the Ministry of Education (MoE), Government of India (Grant No. MoE-STARS/STARS-2/2023-0365) and Science and Engineering Research Board (SERB), Government of India (Grant No. CRG/2021/005548).

References

[1] G. Deysher, J. A. S. Oh, Y. T. Chen, B. Sayahpour, S. Y. Ham, D. Cheng, P. Ridley, A. Cronk, S. W. H. Lin, K. Qian, L. H. B. Nguyen, J. Jang, Y. S. Meng, *Nat. Energy* **2024**, *9*, 1161-1172.

[2] S. Puls, E. Nazmutdinova, F. Kalyk, H. M. Woolley, J. F. Thomsen, Z. Cheng, A. Fauchier-Magnan, A. Gautam, M. Gockeln, S. Y. Ham, M. T. Hasan, M. G. Jeong, D. Hiraoka, J. S. Kim, T. Kutsch, B. Lelotte, P. Minnmann, V. Miß, K. Motohashi, D. L. Nelson, F. Ooms, F. Piccolo, C. Plank, M. Rosner, S. E. Sandoval, E. Schlautmann, R. Schuster, D. Spencer-Jolly, Y. Sun, B. S. Vishnugopi, R. Zhang, H. Zheng, P. Adelhelm, T. Brezesinski, P. G. Bruce, M. Danzer, M. El Kazzi, H. Gasteiger, K. B. Hatzell, A. Hayashi, F. Hippauf, J. Janek, Y. S. Jung, M. T. McDowell, Y. S. Meng, P. P. Mukherjee, S. Ohno, B. Roling, A. Sakuda, J. Schwenzel, X. Sun, C. Villevieille, M. Wagemaker, W. G. Zeier, N. M. Vargas-Barbosa, *Nat. Energy* **2024**, *9*, 1310-1320.

[3] J. Xiao, N. Adelstein, Y. Bi, W. Bian, J. Cabana, C. L. Cobb, Y. Cui, S. J. Dillon, M. M. Doeff, S. M. Islam, K. Leung, M. Li, F. Lin, J. Liu, H. Luo, A. C. Marschilok, Y. S. Meng, Y. Qi, R. Sahore, K. G. Sprenger, R. C. Tenent, M. F. Toney, W. Tong, L. F. Wan, C. Wang, S. E. Weitzner, B. Wu, Y. Xu, *Nat. Energy* **2024**, *9*, 1463-1473.

[4] A. K. Das, M. Badole, H. N. Vasavan, S. Saxena, P. Gami, S. Deswal, P. Kumar, S. Kumar, *Mater. Today Sustain.* **2024**, *26*, 100758.

[5] A. K. Das, M. Badole, H. N. Vasavan, S. Saxena, P. Gami, S. Kumar, *Ceram. Int.* **2023**, *49*, 29719.

[6] T. Kasahara, P. Song, I. Honma, S. Ohno, *Batter. Supercaps* **2025**, *8*.

[7] P. Gami, M. Badole, H. N. Vasavan, A. K. Das, S. Saxena, N. Dagar, V. Srihari, S. Kumar, *J. Power Sources* **2024**, *618*, 235214.

[8] R. Guo, Y. Yang, C. Zhao, F. Huo, J. Xue, J. He, B. Sun, Z. Sun, H. K. Liu, S. X. Dou, *Adv. Funct. Mater.* **2024**, *34*.

[9] X. He, Z. Zhu, G. Wen, S. Lv, S. Yang, T. Hu, Z. Cao, Y. Ji, X. Fu, W. Yang, Y. Wang, *Adv. Mater.* **2024**, *36*.

[10] F. Hu, J. Chen, H. Cao, H. Wang, H. Guo, X. Ouyang, *Adv. Funct. Mater.* **2025**, *35*.

[11] Y. Guo, K. Liu, C. Li, D. Song, H. Zhang, Z. Wang, Y. Yan, L. Zhang, S. Dai, *Adv. Energy Mater.* **2024**, *14*.

[12] A. K. Das, P. Gami, H. N. Vasavan, S. Saxena, N. Dagar, S. Deswal, P. Kumar, S. Kumar, *ACS Appl. Energy Mater.* **2024**, *7*, 8301-8307.

[13] M. T. Ahsan, D. Qiu, Z. Ali, Z. Fang, W. Zhao, T. Shen, Y. Hou, *Adv. Energy Mater.* **2024**, *14*.

[14] X. Kong, R. Gu, Z. Jin, L. Zhang, C. Zhang, W. Xiang, C. Li, K. Zhu, Y. Xu, H. Huang, X. Liu, R. Peng, C. Wang, *Nat. Commun.* **2024**, *15*.

[15] X. Zhao, Z. Fu, X. Zhang, X. Wang, B. Li, D. Zhou, F. Kang, *Energy Environ. Sci.* **2024**, *17*, 2406-2430.

[16] Y. Li, S. Song, H. Kim, K. Nomoto, H. Kim, X. Sun, S. Hori, K. Suzuki, N. Matsui, M. Hirayama, T. Mizoguchi, T. Saito, T. Kamiyama, R. Kanno, *Science* **2023**, *381*, 50-53.

[17] P. Wang, S. Patel, H. Liu, P. H. Chien, X. Feng, L. Gao, B. Chen, J. Liu, Y. Y. Hu, *Adv. Funct. Mater.* **2023**, *33*.

[18] Z. Song, T. Wang, H. Yang, W. H. Kan, Y. Chen, Q. Yu, L. Wang, Y. Zhang, Y. Dai, H. Chen, W. Yin, T. Honda, M. Avdeev, H. Xu, J. Ma, Y. Huang, W. Luo, *Nat. Commun.* **2024**, *15*.

[19] Q. Wang, Y. Zhou, X. Wang, H. Guo, S. Gong, Z. Yao, F. Wu, J. Wang, S. Ganapathy, X. Bai, B. Li, C. Zhao, J. Janek, M. Wagemaker, *Nat. Commun.* **2024**, *15*.

[20] Y. Zeng, B. Ouyang, J. Liu, Y.-W. Byeon, Z. Cai, L. J. Miara, Y. Wang, G. Ceder, *Science* **2022**, *378*, 1320.

[21] A. K. Das, M. Badole, H. N. Vasavan, S. Saxena, P. Gami, N. Dagar, S. Kumar, *J. Energy Storage* **2024**, *94*, 112452.

[22] Y. Liu, M. Lei, C. Lai, J. Meng, X. Wu, Y. Yu, Y. Zhang, C. Li, *Mater. Today* **2022**, *61*, 65-77.

[23] Y. Zhang, J. Meng, K. Chen, Q. Wu, X. Wu, C. Li, *ACS Appl. Mater. Interfaces* **2020**, *12*, 33729-33739.

[24] T. Thompson, J. Wolfenstine, J. L. Allen, M. Johannes, A. Huq, I. N. David, J. Sakamoto, *J. Mater. Chem. A* **2014**, *2*, 13431-13436.

[25] Y. Feng, L. Yang, Z. Yan, D. Zuo, Z. Zhu, L. Zeng, Y. Zhu, J. Wan, *Energy Storage Mater.* **2023**, *63*, 103053.

[26] M. Chen, W. Liu, Y. Wu, Y. Liu, Y. Wang, Z. Chen, *Batter. Supercaps* **2025**, *8*.

[27] Y. Liu, J. Meng, M. Lei, Y. Yu, C. Lai, C. Li, *Adv. Funct. Mater.* **2023**, *33*, 2208013.

[28] H. Wu, J. Hu, S. Yu, C. Li, *Energy Environ. Sci.* **2025**, *18*, 923-936.

[29] S.-K. Jung, H. Gwon, H. Kim, G. Yoon, D. Shin, J. Hong, C. Jung, J.-S. Kim, *Nat. Commun.* **2022**, *13*, 7638.

[30] B. Ouyang, Y. Zeng, *Nat. Commun.* **2024**, *15*, 973.

[31] K.-F. Ren, H. Liu, J.-X. Guo, X. Sun, F. Jiang, C. Guo, W. Bao, F. Yu, G. Kalimuldina, L. Kong, X.-B. Cheng, J. Li, *ACS Energy Lett.* **2024**, *9*, 2960-2980.

[32] A. Coelho, *J. Appl. Crystallogr.* **2018**, *51*, 210.

[33] F. Ciucci, C. Chen, *Electrochim. Acta* **2015**, *167*, 439-454.

[34] T. H. Wan, M. Saccoccio, C. Chen, F. Ciucci, *Electrochim. Acta* **2015**, *184*, 483-499.

[35] M. B. Effat, F. Ciucci, *Electrochim. Acta* **2017**, *247*, 1117-1129.

[36] J. Liu, T. H. Wan, F. Ciucci, *Electrochim. Acta* **2020**, *357*, 136864.

[37] Y. Chen, T. Wang, H. Chen, W. H. Kan, W. Yin, Z. Song, C. Wang, J. Ma, W. Luo, Y. Huang, *Matter* **2023**, *6*, 1530-1541.

[38] F. Okur, H. Zhang, J. F. Baumgärtner, J. Sivavec, M. Klimpel, G. P. Wasser, R. Dubey, L. P. H. Jeurgens, D. Chernyshov, W. van Beek, K. V. Kravchyk, M. V. Kovalenko, *Adv. Sci.* **2025**, *12*, 2412370.

[39] S. Li, J. Lin, M. Schaller, S. Indris, X. Zhang, T. Brezesinski, C.-W. Nan, S. Wang, F. Strauss, *Angew. Chem. Int. Ed.* **2023**, *62*, e202314155.

[40] R. Murugan, V. Thangadurai, W. Weppner, *Angew. Chem. Int. Ed.* **2007**, *46*, 7778.

[41] M. P. O'Callaghan, E. J. Cussen, *Chem. Commun.* **2007**, *20*, 2048.

[42] S. Kripotou, C. Psylla, K. Kyriakos, K. N. Raftopoulos, J. Zhao, G. Zhang, S. Pispas, C. M. Papadakis, A. Kyritsis, *Macromolecules* **2016**, *49*, 5963-5977.

Table of Contents (ToC)

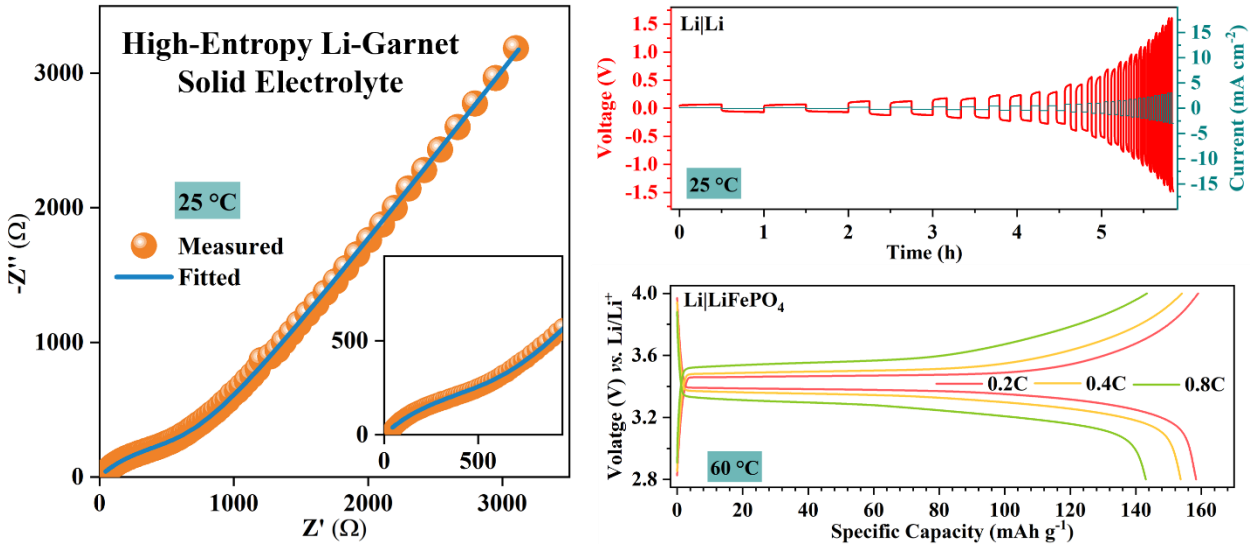

The compositionally tuned high-entropy Li-garnet solid electrolyte exhibited high conductivity and excellent electrochemical performance in symmetric and full cells.

[Supporting Information]

COMPOSITIONALLY TUNED HIGH-ENTROPY LI-GARNET ELECTROLYTE FOR ADVANCED SOLID-STATE BATTERIES

Asish Kumar Das[a,*] and Sunil Kumar[a,**]

[a]Department of Metallurgical Engineering and Materials Science, Indian Institute of Technology Indore, Simrol, 453552, India

**Corresponding author E-mail: sunil@iiti.ac.in

*Corresponding author E-mail: phd2201105011@iiti.ac.in

Table S1: *Results of Rietveld refinement of powder X-ray diffraction data of HEG powder calcined at 950 °C.*

Site	Wyckoff position	x	y	z	Atom	Occupancy
Li1	24d	0.375	0	0.25	Li^{+1}	0.468
Li2	96h	0.69(1)	0.59(7)	0.11(4)	Li^{+1}	0.466
La	24c	0.125	0	0.25	La^{+3}	1
Zr	16a	0	0	0	Zr^{+4}	0.25
Ta	16a	0	0	0	Ta^{+5}	0.25
Nb	16a	0	0	0	Nb^{+5}	0.25
Hf	16a	0	0	0	Hf^{+4}	0.125
Sc	16a	0	0	0	Sc^{+3}	0.125
O	96h	0.28(5)	0.09(8)	0.19(7)	O^{-2}	1

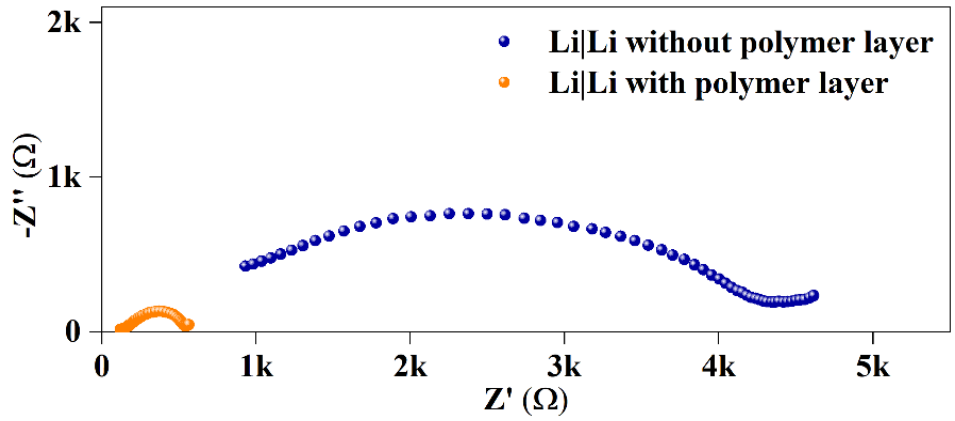

Figure S6: Nyquist plots of Li | HEG | Li cells with polymer buffer layer at lithium metal interface before and after cycling for 550 cycles.

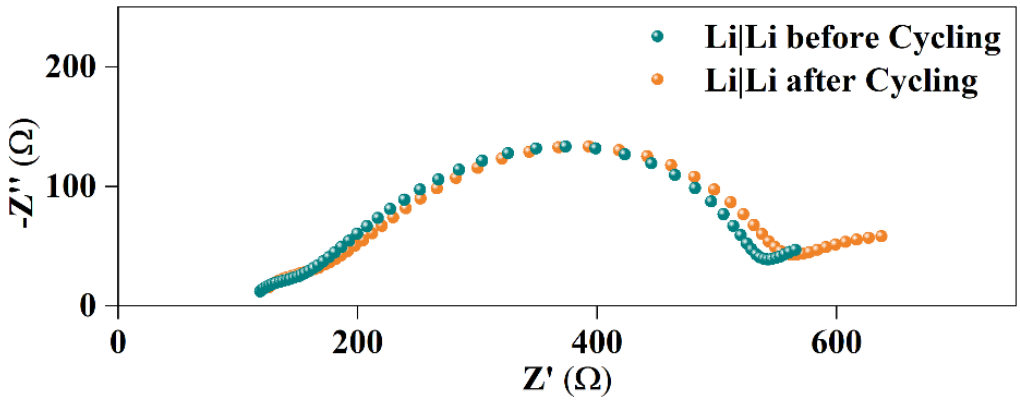

Figure S7: Nyquist plots of lithium symmetric cells without and with PEO/LiTFSI polymer layer at the lithium metal interface.

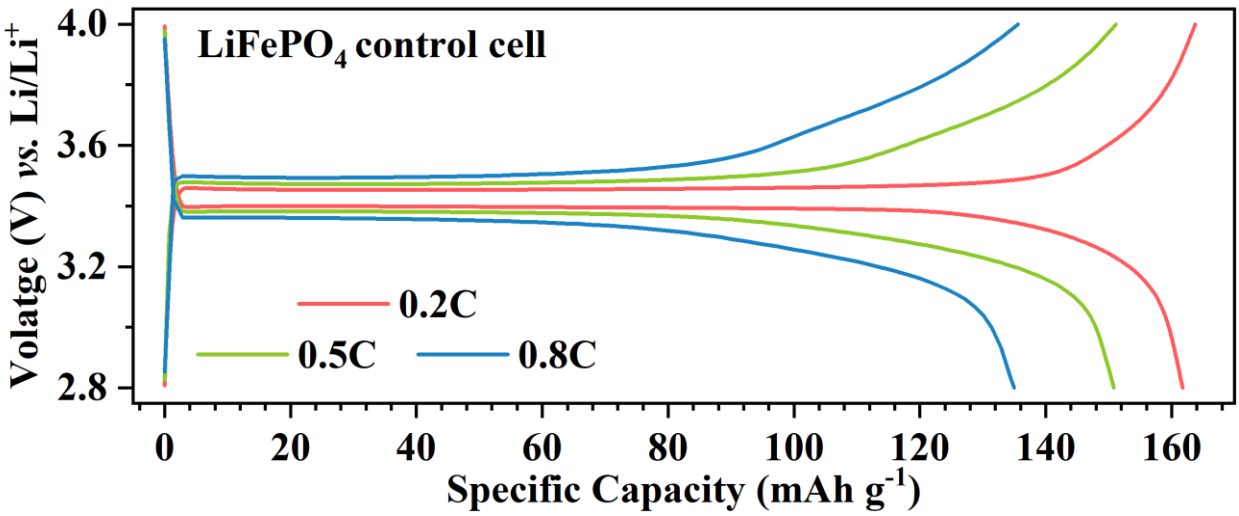

Figure S8: The specific capacity-voltage curves of the $LiFePO_4$ control cell at different C-rates at 25 °C.

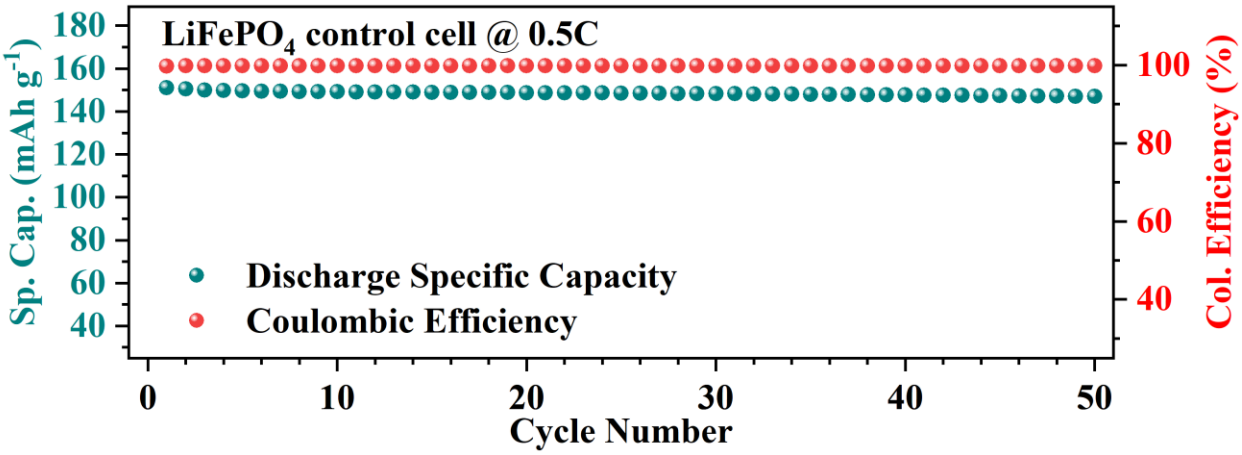

Figure S9: The long-term cyclability of $LiFePO_4$ control cell at 0.5C at 25 °C.

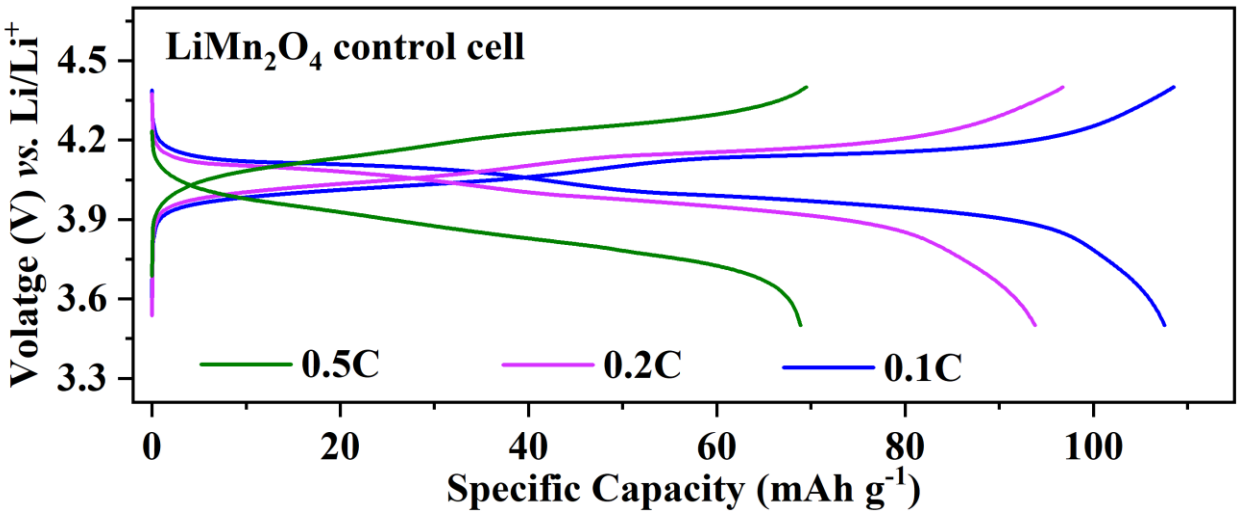

Figure S10: The specific capacity-voltage curves of the $LiMn_2O_4$ control cell at different C-rates at 25 °C.

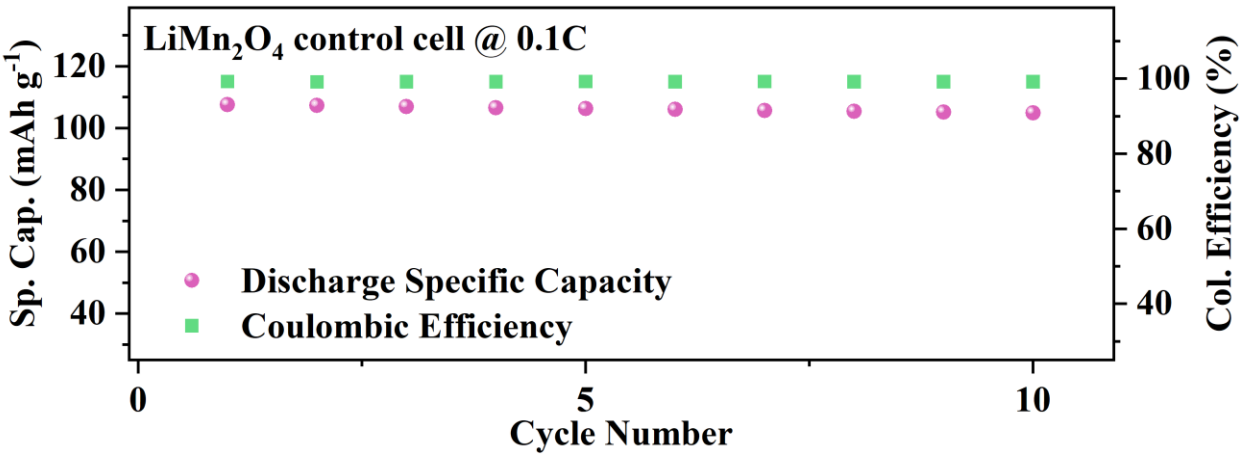

Figure S11: The long-term cyclability of $LiMn_2O_4$ control cell at 0.1C at 25 °C.